PCCP

Accepted Manuscript

ROYAL SOCIETY OF CHEMISTRY

www.rsc.org/pccp

Cite this: DOI: 10.1039/xxxxxxxxxx

Enhancing the Carrier Thermalization Time in Organometallic Perovskites by Halide Mixing

M.E. Madjet [a], A. V. Akimov[b], F. El-Mellouhi,[a], G. Berdiyorov[a], S. Ashhab[a], N. Tabet[a] and S. Kais[a,c]

Received Date
Accepted Date

DOI: 10.1039/xxxxxxxxxx

www.rsc.org/journalname

Hybrid metal-organic halide perovskites have recently attracted a great deal of attention because of their interesting electronic, optical and transport properties, which make them promising materials for high-performance, low-cost solar cells. Fundamental understanding of the formation mechanisms and dynamics of photoinduced charge carriers is essential for increasing the performance of perovskite solar cell devices. For example, a significant amount of absorbed solar energy is lost as a result of carrier thermalization. This energy can be harnessed by extracting the hot carriers before they cool down to the band edges. Although, such hot carrier collection is experimentally challenging, theoretical investigations based on time-dependent methods can guide future experimental research by providing insights on the thermalization process. Here, we perform *ab initio* nonadiabatic molecular dynamics simulations to study non-radiative recombination dynamics of charge carriers in the hybrid halide perovskites. We find that the carrier relaxation time can be considerably increased by mixing halogen atoms in the perovskite materials. These findings show that simple approaches could be adopted to slow down the thermalization process of hot carriers in perovskite materials.

Hybrid metal-organic halide perovskites (HMOHPs), such as methylammonium (MA) lead iodide ($CH_3NH_3PbI_3$ or $MAPbI_3$) have received a revival of interest in recent years as promising absorber materials for solar energy applications. Their remarkable optical properties also make them very promising for use in light emitting devices, such as lasers [1]. Solar power conversion efficiencies of more than 20% reported for these materials [2] (see Refs.[3–9] for reviews) qualify them as a promising potential alternative to silicon in the photovoltaics industry. Moreover, lead halide perovskite solar cells can be fabricated using low-temperature solution processing and inkjet printing methods that would result in a low manufacturing cost. The high photovoltaic efficiency in this class of materials is mainly related to the strong light absorption across much of the solar spectrum [10–14], the relatively long diffusion lengths of charge carriers [15–19] and the high carrier mobility [20–25] associated with a low sensitivity to defects [26,27]. In addition, structural and electronic properties of MAPbI3 have been improved by chemical engineering, e.g., through mixing halogen atoms[19,28–38]. Halogen mixing is believed to improve the stability of the material [30,39] and prevent the formation of key structural defects [40]. Improved charge-carrier mobility and electron and hole diffusion lengths have also been observed in mixed-halide perovskites [15,16,28,41–43].

For the various projected applications of HMOHPs, a thorough experimental and theoretical understanding of the processes leading to charge carrier formation, charge density dynamics, band filling, defect migration as well as spectral broadening mechanisms, is essential [44–48]. Recently, Miyata et al.[50] determined from experimental results that the exciton binding energy for the orthorhombic phase of $MAPbI_3$ is 16 meV. They also showed that

[a] *Qatar Environment and Energy Research Institute, Hamad Bin Khalifa University, Qatar Foundation, PO Box 5825, Doha, Qatar ; E-mail: mmadjet@qf.org.qa*
[b] *Department of Chemistry, University at Buffalo, Buffalo, State University of New York, NY 14260-3000; E-mail:. alexeyak@buffalo.edu*
[c] *Department of Chemistry, Physics and Birck Nanotechnology Center, Purdue University, West Lafayette, IN 47907 USA.*

for the tetragonal phase the binding energy is on the order of only a few millielectron volts. In fact, the presence of photo-induced free carriers has been confirmed in these materials[16,49], pointing to weak Coulomb interactions between electrons and holes in these systems. These findings validate the previously proposed hypothesis of spontaneous free carrier generation following light absorption by perovskite materials at room temperature. However, many fundamental processes related to the photophysics, such as the properties of photo-excited electrons, remain nearly unexplored. In this context, a theoretical investigation based on time-dependent methods is needed to understand in more detail recent experimental findings [51] and also to guide future experimental investigations.

In photovoltaic cells, the photoexcitation of electrons from the valence band to the conduction band generally results in the formation of hot electrons and holes. These carriers lose their kinetic energy by cooling down to the band edges. This thermalization process occurs on a femtoseconds timescale. The carrier recombination process in absorbing material of direct gap is dominated by the electron-hole radiative recombination and occurs on a time scale that is typically longer than a nanosecond, meaning that the recombination process can be ignored at the timescale of relaxation dynamics. Ideally, and for efficient device operation, extracting photo-generated charge carriers with minimal energy and carrier losses is desirable. However, the slowing down of hot carrier relaxation dynamics due to halogen-mixing will probably have a negligible effects on charge separation. We would like to point out that the overall charge separation model is beyond the scope of the present work.

Harvesting the energy of hot carriers before it is converted into heat would enhance the power conversion efficiency (PCE)[52] of a solar cell through an increase in the carrier collection efficiency and the open circuit voltage (Voc). Finding ways to increase the carrier lifetime would also provide a path to control of the relaxation dynamics, which would be favourable for photovoltaic applications. Various approaches have been suggested in the literature, including the use of quantum dots to slow down the thermalization process[53] or erbium ions in combination with silicon nanocrystals to generate infrared photons[54]. However the successful implementation of these ideas in a working device remains a challenge. In a recent experiment, Yang et al.[55] found that the thermalization in perovskite can slow down by about three orders of magnitudes due to hot-phonon bottleneck at high injection levels. A slow cooling dynamics and a phonon bottleneck effect were also resolved by Price et al.[56]. They observed that at higher excitation densities, a phonon bottleneck effect becomes more pronounced that substantially slows hot carrier cooling. Consequently, due to the practical and fundamental importance of electron and hole relaxation dynamics in photovoltaic materials in general and in perovskites in particular, it is crucial to understand how this process depends on the perovskite structure and what are the timescales for these processes, which might provide guidance for better design of hot-carrier devise architecture.

Recently, there have been a number of experimental and theoretical studies performed in order to gain insight into the carrier transport and hot carrier relaxation processes in organic-inorganic perovskite materials[15,51,57–66]. Using femtosecond transient absorption spectroscopy, Manser and Kamat[66] reported the characterisation of the ultrafast relaxation processes and charge accumulation in $MAPbI_3$ due to the thermalization of hot carriers that start filling the states near the band edges. This results in an increase of the band gap and more energetic photons are required to generate additional charge carriers. Sum and Mathews[5] reviewed the basic working mechanisms of perovskite solar cells linked to their fundamental photo physics and intrinsic properties. The radiative recombination of free carriers occurs over a period of several nanoseconds by emitting strong and broad photoluminescence (PL) spectra around the band gap energy. Recent experiments have shown that the Cl-doped $MAPbI_3$ perovskite has a long PL lifetime of a few hundred nanoseconds. However the direct effect of the Cl^- ions is still a matter of debate.

In the present study, we will investigate the effect of halide mixing on carrier relaxation dynamics. We use non-adiabatic molecular dynamics (NA-MD) combined with time-dependent Kohn-Sham (TD-KS) density functional theory to study the non-radiative electron and hole relaxation dynamics in lead-halide perovskites $CH_3NH_3PbX_3$ (X=I, Cl, Br) and show how the relaxation time depends on the structure and composition of the system. Since the charge carrier relaxation is driven by inelastic electron-phonon scattering[44], we also discuss the vibrational modes that drive the relaxation of hot electrons and holes to the band edges. Our findings show that simpler approaches could be adopted to slow down the thermalization process of hot carriers based on careful tailoring of the composition and structure of the absorbing layers such as using mixed-halide materials.

1 Computational methodology

Our approach for studying excited state dynamics is based on Kohn-Sham density-functional theory (KS-DFT), which provides a good description of the non-adiabatic dynamics of extended systems, while remaining computationally tractable. It is known that the GW approximation is the most rigorous approach for studying excited state properties of periodic systems including many-electron effects. Including the effect of spin-orbit coupling would also allow a more accurate description of electronic, optical and transport properties of organic-inorganic perovskite materials[67]. However, for long molecular dynamics simulations involving excited states and nonadiabatic dynamics, using GW and including spin-orbit coupling becomes computationally extremely demanding. The KS-DFT based method offers an alternative com-

putational framework making it possible to propagate the nonadiabatic molecular dynamics of extended systems at an affordable computational cost and providing a qualitatively good description of the dynamics. In the following we give a brief description of the nonadiabatic molecular dynamics formalism used in the present study. We use a mixed quantum-classical trajectory surface hopping (TSH) approach[68], which represents one of the most promising and computationally feasible methods for extended systems. In this approach, the electrons are described quantum mechanically by solving the Schrödinger equation and the nuclei are treated classically by solving the classical Newton equations. The integration of the classical equations is done by using the velocity Verlet algorithm[69,70]. Since both electrons and holes are described quantum mechanically, this approximation is appropriate to study charge carrier transport properties. The electronic wave function can be expressed in terms of the adiabatic states $\Phi_i(\vec{r};\vec{R}(t))$ by the following expression

$$\Psi(\vec{r},\vec{R},t) = \sum_i c_i(t)\Phi_i(\vec{r};\vec{R}(t)), \tag{1}$$

where $\vec{r}$ and $\vec{R}$ denote collective electronic and nuclear coordinates, respectively. The expansion coefficients $c_i(t)$ are determined by propagating the time-dependent Schrödinger equation

$$i\hbar\frac{dc_i(t)}{dt} = \sum_j c_j(t)[H_{ij} - i\hbar\dot{\vec{R}}\cdot\vec{d}_{ij}], \tag{2}$$

where $\vec{d}_{ij}$ are the derivative coupling matrix elements between states i and j. The TSH scheme requires the computation of the nonadiabatic electronic coupling (NAC) between the KS orbitals driven by the ionic motion as

$$\sigma_{ij} = \dot{\vec{R}}\cdot\vec{d}_{ij} = \dot{\vec{R}}\cdot\langle\Phi_i(\vec{r};\vec{R}(t))|\vec{\nabla}_{\vec{R}}|\Phi_j(\vec{r};\vec{R}(t))\rangle. \tag{3}$$

In the adiabatic representation the Hamiltonian matrix H_{ij} is diagonal and Eq.2 simplifies to

$$i\hbar\frac{dc_i(t)}{dt} = c_i(t)\varepsilon_i - i\hbar\sum_j c_j\sigma_{ij}, \tag{4}$$

where ε_i is the energy of the i^{th} KS orbital. For the evaluation of the NAC term, we use the finite difference scheme proposed by Hammes-Schiffer and Tully[71], where the σ_{ij} is expressed in terms of the overlap between the wave functions at t and $t+dt$

$$\begin{aligned}\sigma_{ij}(t+dt/2) &= \frac{1}{2dt}[\langle\Phi_i(\vec{r};\vec{R}(t))|\Phi_j(\vec{r};\vec{R}(t+dt))\rangle \\ &- \langle\Phi_i(\vec{r};\vec{R}(t+dt))|\Phi_j(\vec{r};\vec{R}(t))\rangle]\end{aligned} \tag{5}$$

Note that the NAC between the states i and j is evaluated at every time step of the molecular dynamics (MD) trajectory. The transition dipole moments can be computed using the following relation:

$$\vec{\mu}_{ij} \equiv e\langle\Phi_i|\vec{r}|\Phi_j\rangle \tag{6}$$

In the surface hopping formalism, the photo-excited electron is assumed to be in one of the adiabatic KS state at any point in time t, but it has the possibility to stochastically hop from one state to another. The hopping probability from state i to j is given by[68]:

$$P_{i\to j} = 2\int_t^{t+dt} d\tau\frac{Re[c_i(\tau)^* c_j(\tau)\sigma_{ij}(\tau)]}{c_i(\tau)c_i^*(\tau)}, \tag{7}$$

where dt and $d\tau$ are the electronic and nuclear integration time steps, respectively. In order to calculate the hopping probability $P_{i\to j}$, the coefficients c_i are obtained by numerical integration of the differential equation Eq. 4. Note that the population of a state i is given by $|c_i|^2$. It is worth mentioning that the quantities $P_{i\to j}$ only determine the state of the system with respect to possible hops. If the quantity $P_{i\to j}$ is negative, no hops from the state i to the state j are possible. In this case, the hopping probability is set to zero. If the quantity $P_{i\to j}$ is positive, more population must be transferred to the state j, which can be accommodated via a surface hop. In this case the quantity is associated with the hopping probability. Therefore, the final transition probability is defined as

$$g_{ij} = \max(P_{i\to j}, 0). \tag{8}$$

The relaxation dynamics is computed using the fewest-switches surface-hopping (FSSH)[68] technique adapted to the classical path approximation (CPA), as explained elsewhere[73,74] . The FSSH probabilities are related to the flux of state populations, rather than the state populations themselves. This property minimizes the number of hops, giving rise to the term "fewest switches". A random number ξ is generated ($0 \le \xi \le 1$) at each time step and a hop from the state i to the state k is performed if:

$$\sum_{j=1}^{k} g_{ij} < \xi < \sum_{j=1}^{k+1} g_{ij}. \tag{9}$$

In the original FSSH formulation, after a hop to a new state, the nuclear velocities are rescaled along the NAC coupling direction to conserve the total energy. In the present FSSH-CPA, no such velocity rescaling is needed. Instead, it is replaced by scaling the transition probabilities by a Botztmann factor (See Ref.[74]). More details about the NA-MD methodology can be found in Refs.[72,75]. Note that electron-hole interactions are not included in our approach. However, knowing that the exciton binding energy in hybrid perovskites is only a few meV[50] (due to the large value of the real part of the static dielectric constant), one could expect that exciton effects on the thermalization process of hot carriers will be small. To study hot electron and hole relaxation processes in the lead halide perovskites, we perform nonadiabatic molecular dynamics simulations using a combination of the PYthon eXtension for Ab Initio Dynamics (PYXAID)[73,74] package for quan-

tum dynamics simulations interfaced with the Quantum Espresso (QE) electronic structure code[73]. Quantum calculations employ DFT with the PBE exchange-correlation functional[76,77] as implemented in the QE package[78]. Following the standard procedure, the effects of the core electrons are described by atomic pseudopotentials generated independently for all atoms included in the calculations. Norm-conserving pseudopotentials are used to describe the core-valence interaction. The valence electrons are described using plane waves and a cutoff of 50 Ry and 530 Ry, respectively, for the wavefunctions and the density expansion.

The computations are performed in three steps, as described elsewhere[73,74]. In the first step, a full optimization of the cell volume and atomic positions of the perovskite ground state structures are performed until energy and forces have converged to variations smaller than 10^{-4} eV and 0.01 eV/Å, respectively. Subsequently, the system is thermalized by running up to 7 ps ab initio MD simulation in the canonical NVT ensemble. The velocity Verlet[69] algorithm with a time step of 1 fs is utilized to propagate the nuclear coordinates, and the electronic amplitude is propagated with a time step of 0.1 fs. The Andersen (collision) thermostat[79] is used to maintain the average temperature at 300 K, and a collision frequency parameter of 0.05 fs^{-1} is used. In the second step of our computations, the electronic structure of the evolving system is recomputed for each time step along the MD trajectory. The computed KS energies and orbitals are utilized to obtain the nonadiabatic (NA) couplings using Eq. 5 and to form the vibronic Hamiltonian matrices as well as to compute the transition dipole matrix elements from Eq. 6. This time-dependent information is stored and used to perform the subsequent NA-MD simulations and data analysis. According to the CPA employed in the present study, the evolution of electronic degrees of freedom follows the ground-state evolution of the nuclei, but the nuclear dynamics remains unaffected by the electronic transitions. This approximation is justified by a relatively rigid structure of the perovskite materials and by the absence of significant structural changes upon photoexcitation. We consider perovskites in the tetragonal room temperature phase where the valence band maximum and the conduction band minimum are located at the Γ point. Also only the Γ point of the Brillouin zone is used in the excited state dynamics. In the third step of our computations, the NA-MD simulations are performed. To study the hot hole and hot electron relaxation processes, we have chosen a minimal basis of adiabatic excited states represented by excited Slater determinants constructed from the KS orbitals[80]. In the present approach, the time-dependent electron wave function of the system is not based on a many-body all-electron wave function but relies on single-particle orbitals. Future studies going beyond the single-particle approximation by including the electron-electron interactions will be useful to investigate the quasiparticle effects on the relaxation of hot carriers. The last approximation was already used in a previous theoretical work to investigate the relaxation of hot carriers in silicon[81].

To obtain reliable statistics, we average the results over 1000 stochastic realizations of the surface hopping algorithms and over 20 starting geometries. To avoid numerical artifacts associated with incomplete thermalization, we exclude the first 1 ps of the computed MD trajectory from our sampling domain. To understand the charge transfer and energy relaxation dynamics, we compute the average populations of several excited electronic and hole states. The time-dependent population of each state can be calculated by:

$$Pop_i^{SH}(t) = \frac{N_i(t)}{N} \tag{10}$$

where N_i (t) is the number of SH trajectories in electronic state i at time t and N is the total number of trajectories in the ensemble. The average value of energy of a carrier (electron or hole) can be computed as a function of time as:

$$E(t) = \langle \sum_i E_i \; Pop_i^{SH}(t) \rangle_{ens} \tag{11}$$

where E_i(t) denotes the energy of the basis set i and $<\cdot>_{ens}$ is the ensemble average (over initial configurations and realizations of the surface hopping trajectories).

2 Results and discussion

As a typical example, we consider a unit cell of the tetragonal phase of $MAPbI_3$, which is the room temperature phase of the material. After optimization, we systematically replaced the iodide atoms with chlorine or bromine atoms at both the axial and the equatorial octahedral positions and relaxed the system further to its lowest-energy configuration. As an example, we present results for a single Cl and Br substituted systems (which corresponds to 8% doping) at the equatorial site. The choice of the equatorial site substitution was motivated by the fact that it is energetically more favorable (according to our total energy calculations) and is convenient because of the recent finding of Zheng et al.[43] that equatorial halide substitution results in enhanced transport properties of the material. Further investigations are needed to study the effect of the doping site and also the effect of the concentration on hot carrier thermalization.

The systems will be referred to as T-$MAPbI_3$, T-$MAPbI_3$(Cl) T-$MAPbI_3$(Br) where the letter T refers to the tetragonal phase and the symbol between parentheses refers to the species substituting one iodine atom in the unit cell.

Structural properties of the fully relaxed systems are given in Table 1 to demonstrate the structural changes induced by halide mixing. Worth noting that geometry optimization was done using a dense mesh of k-points (8x8x8). The calculated lattice parameters for $MAPbI_3$ were a= 8.98 Å and c= 12.94 Å which are comparable to experimental results (a=8.86 Å and c=12.66 Å)[82].

Full iodine substitution leads to smaller lattice parameters in the three directions and one iodine substitution leads to a smaller a parameter (see Table 1). The optimized lattice parameters for T-$MAPbI_3$(Cl) and T-$MAPbI_3$(Br) are very similar.

2.1 Energy relaxation

We start our analysis by considering the relaxation of the ensemble-averaged excited state energy (Eq.11) after the system is excited by a photon with energy larger than the band gap of the material. To study the energy relaxation of hot electrons and hot holes separately, we either excited electrons from the valence band maximum (VBM) to states in the conduction band with energy ΔE_e above the conduction band minimum (CBM) or promoted electrons from states with energy ΔE_h below the VBM to the CBM (see Fig. 1 for the definitions of ΔE_e and ΔE_h). The energy values of ΔE_e (ΔE_h) for CBM+n (VBM-n) are listed in Table S3. We should mention here that these values are not for the optimized structures but for structures used as initial structures for the nonadiabatic dynamics as the first 1 ps of the computed MD trajectory was excluded. The non-radiative relaxation occurs via the conversion of excitation energy to thermal energy driven by electron-phonon interactions, as illustrated in Fig.1. The relaxation process is described using the NA-MD in combination with Tully's surface hopping method[68]. The time-dependent population is obtained by averaging over 20 initial configurations and 1000 surface hopping (SH) trajectories for each configuration. Non-adiabatic transitions starting from the six and ten lowest excited states were included in electron and hole relaxation dynamics, respectively.

Table 1 Calculated lattice parameters (Å) for different perovskite systems.

	$MAPbI_3$	$MAPbCl_3$	$MAPbBr_3$	T-$MAPbI_3$(Cl)	T-$MAPbI_3$(Br)
a	8.98	8.12	8.65	8.80	8.83
c	12.94	11.36	12.77	12.86	12.89

Figure 2 presents the time evolution of the KS population-weighted energies (average excitation energies) in $MAPbI_3$ when the system is initially excited to different states with ΔE less than 0.5 eV above the CBM (Fig. 2a) and below the VBM (Fig. 2b) for hot electrons and hot holes, respectively. The most profound feature in the relaxation processes observed in the system is that, once excited to higher energy states, the average excitation energy for electrons clearly relaxes with a slower rate as compared to holes. The hole energies are nearly at zero after 1 ps, indicating that almost all holes have decayed to the VBM. The population-weighted energy of electrons, on the other hand, exhibits much slower decay. For example, the CBM+5 state (ΔE=0.6141 eV) is not fully relaxed even after 2500 fs (Fig.2a). This difference in the non-radiative relaxation dynamics of hot electrons and hot holes

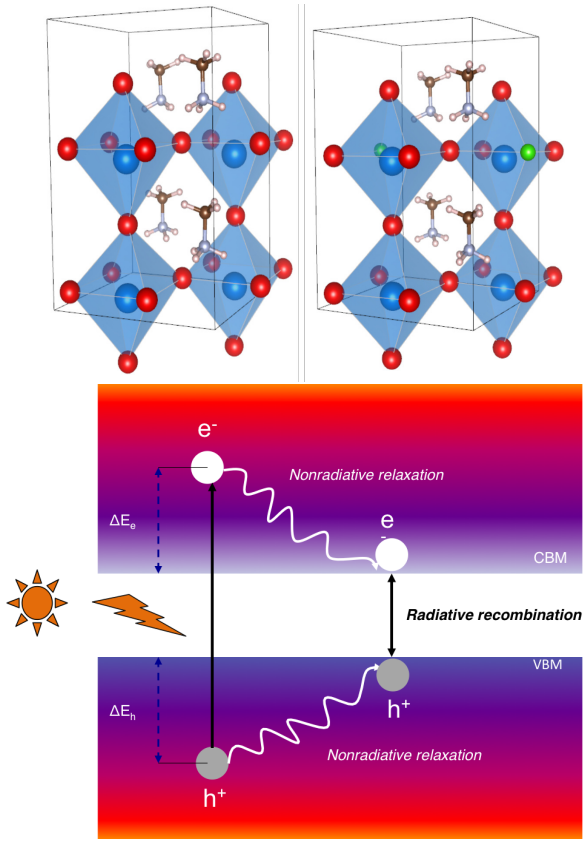

Fig. 1 Upper panel: Optimized geometries of $MAPbI_3$ (a) and chloride-doped $MAPbI_3$(Cl) (b). Lower panel: Schematic diagram representing hot electron and hot hole relaxation dynamics in perovskite materials.

can originate from the difference between the DOSs for electrons and holes [90] and different nonadiabatic coupling between the states in the conduction and valence bands. In the next section we will study the NAC between different states both in the conduction and valence bands.

2.2 Nonadiabatic couplings

To understand the different relaxation processes of electrons and holes, we have calculated nonadiabatic couplings between the energy states both in the valence and conduction bands. Figure 3 shows the results for $MAPbI_3$ and T-$MAPbI_3$ (Cl), which are averaged over 5 ps MD trajectories. The transitions along the subdiagonal lines are strong, indicating that non-radiative transitions are most likely to occur between adjacent states. On the contrary, the nonadiabatic coupling is very small between states that are separated by a large energy spacing. This behavior is expected, knowing that the strength of the NA coupling is inversely proportional to the difference between the energy levels. Tables S1 and S2 in the SI show the couplings between some states in the con-

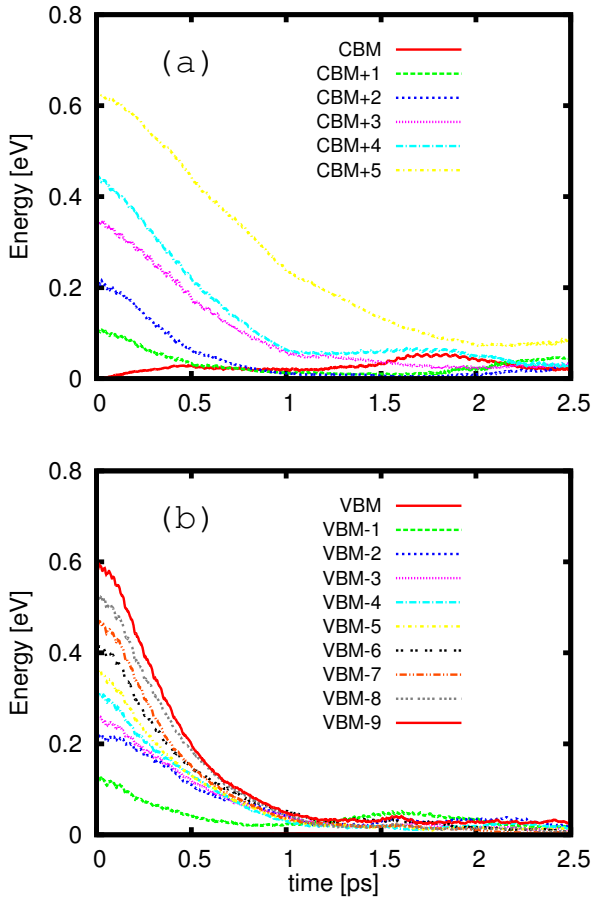

Fig. 2 Time evolution of the KS population-weighted energies after initial excitations to different excited states for electrons (a) and holes (b) in $MAPbI_3$.

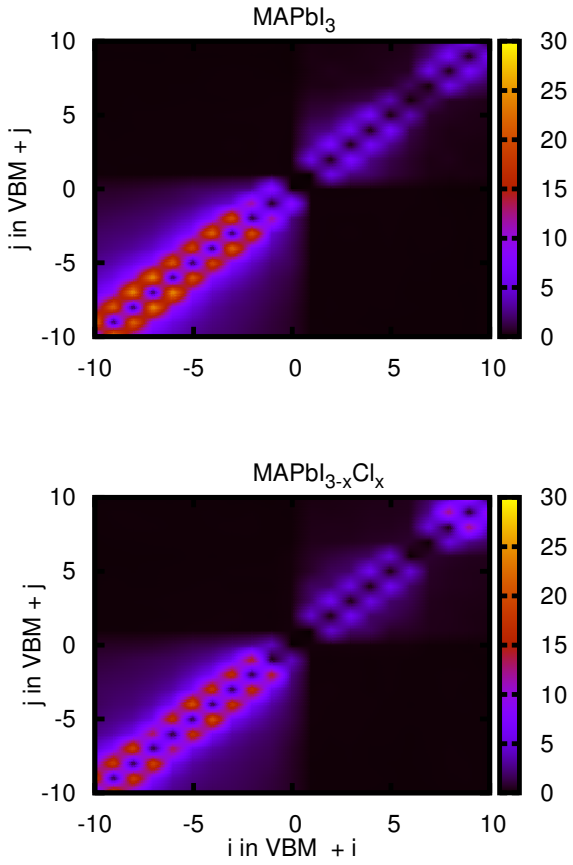

Fig. 3 Visualization of the average magnitude of the nonadiabatic couplings (in units of meV) between states in the space of KS orbital indices for T-$MAPbI_3$ and T-$MAPbI_3$ (Cl). Here i=0 means the VBM state, i=1 means the CBM state, and other states are assigned indices based on these two reference points.

duction and valence bands for $MAPbI_3$ and $MAPbI_3$(Cl), respectively. Clearly, the strongest coupling occurs between adjacent states in the both bands. As a general trend, for all the considered systems, the coupling between hole states is larger than that between electronic states. We should mention here that the NA coupling between valence states close to the VBM is weaker than the coupling between the states deep inside the valance band (see Fig. 3). For example, in the case of the $MAPbI_3$ system, the couplings between VBM/VBM-1 and between VBM-1/VBM-2 states are 8.7 and 12.5 meV, respectively. Whereas, the couplings between VBM-6/VBM-7 and between VBM-7/VBM-8 states are 25.9 and 22.9 meV, respectively. This of course will have an impact on slowing down the hole relaxation when it is close to the VBM. The same trend is also seen for NA couplings for $MAPbI_3$(Cl). However, halide mixing results in a significant reduction of the non adiabatic coupling between different states. This in turn increases the non radiative relaxation time of the charge carriers, which we will discuss in the next section and show how the NA coupling controls hot carrier relaxation.

2.3 Electronic population decay

Figure 4 shows the time dependence of the electronic population for all three systems, when the system is excited to CBM+4 state. Note that, for the sake of better illustration, we present the sum of the two lowest state populations (i.e. CBM and CBM+1) as a new lowest state population (CBM01). For the full iodide system (Fig. 4a), it takes about 1 ps for the depopulation of the initial state and full population of the new lowest state. This population transfer happens through a sequence of nonadiabatic transitions between neighbouring excited states before being transferred to the lowest excited states (CBM). The pathway for this sequential decay is determined by the strong nonadiabatic coupling between the excited states discussed in the previous section. However, direct population transfer between the initial state and the lower

excited states is also possible because of the non-vanishing NA coupling between these two states. This indicates that the mechanism of carrier relaxation goes beyond the sequential stepwise fashion and may include several relaxation channels activated in parallel.

The situation changes considerably with the introduction of a single Cl substituent into the system (Fig. 4 (b)). The time for both depopulation of the initial state and the full population of the lowest state increases by more than a factor of 2. This is due to the decreased coupling between the electronic states discussed earlier (see Fig. 3). However, the Br substituted system T-MAPbI$_3$(Br) does not show such a suppressed decay in the CBM+4 carrier population (Fig. 4 (c)) and remains comparable to T-MAPbI$_3$. The main difference is the population of CBM+3 state that overtakes the other populations at about 0.5 ps before it decays completely at about 2 ps. Similar results have been observed when the system is initially excited to the other states.

The time evolution of the hole state populations is shown in Figure 5 when all the systems are initially excited to the VBM-8 state. For MAPbI$_3$, this initial state corresponds to an energy of about 0.51 eV below the VBM. As we can see from the three panels in the figure, an ultrafast decay is observed for the hole population in the three systems. The initial state is completely depopulated within 0.5 ps, which represents a faster decay process than the decay of the electron population (see Figure 4). The simultaneous rise in the populations of multiple intermediate states is an indication that several relaxation channels contribute to the relaxation process. After 1.5 ps, the initial hole population is almost completely transferred to the edge of the valence band for all three systems.

To get an estimation of the relaxation time, the electron and hole initial-state **de**population is fitted by an exponential decay function exp(-t/τ), where τ is the relaxation time. We also fitted the time-dependent populations of the two lowest states CBM01 by the function 1-exp($-t/\tau'$). As an example, we show in Fig. 6 the population time τ' of the lowest electron and hole states (CBM01 and VBM01) as a function of excited state energy ΔE for T-MAPbI$_3$ (open and filled circles) and T-MAPbI$_3$(Cl) (open and filled squares). For the other considered systems see Fig. S1. Note that in these figures we plotted the hot carrier relaxation time as a function of excitation energy rather than in terms of excited state number. This is because the considered systems have different band structures and different absorption spectra. It can be seen from this figure that the hot electron (with $\Delta E < 0.5$ eV) relaxation in MAPbI$_3$ perovskites occurs between 350 fs and 850 fs, which is in good agreement with the findings of the recent experiments[51]. The hot-hole relaxation time is smaller as compared to the hot-electron relaxation time, except for very small excitation energies. The difference between those two population times becomes more pronounced at larger excitation energies. For T-

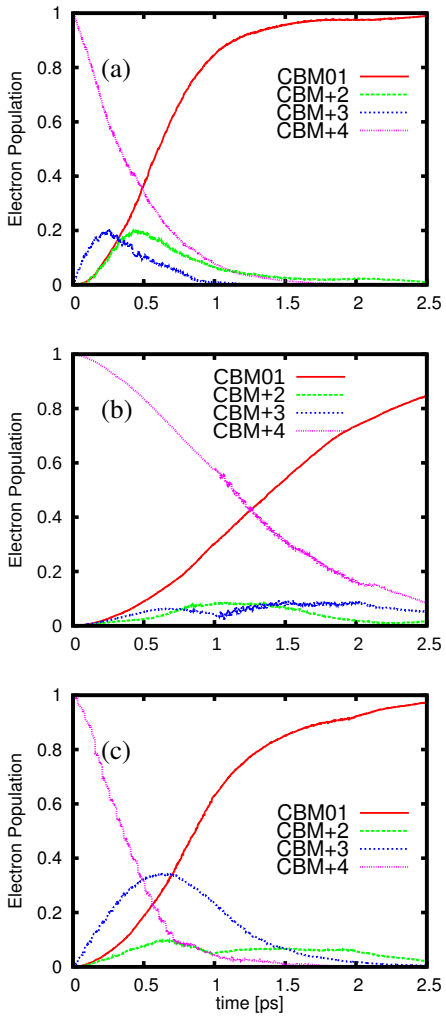

Fig. 4 Time evolution of the electronic state populations after initial excitation to the excited state CBM+4 for T-MAPbI$_3$ (a), T-MAPbI$_3$(Cl)(b) , and T-MAPbI$_3$(Br) (c).

MAPbI$_3$ and for energies smaller than 0.3 eV, the population time for electrons and holes are very similar. For $\Delta E \approx 0.46$ eV, $\tau'_e \approx$ 700 fs compared to $\tau'_h \approx 600$ fs. However, at an excitation energy close to 0.62 eV, the population time for electrons is about 1300 fs compared to 650 fs for holes. Cl substitution results in significant increase in the relaxation time of hot electrons (see filled squares in Fig. 6). For example, at E $\approx$ 0.34 eV, the electronic population is transferred to the conduction band edge of T-MAPbI$_3$ within 650 fs, whereas the population time of the lowest state in the Cl-substituted system is more than 1 ps. The depopulation times of the excited states are also increase by the Cl substitution. For example, at $\Delta E = 0.32$ eV the electrons in the full iodide system relaxes within $\sim$ 400 fs, whereas for the T-MAPbI$_3$(Cl) system it increases to about 980 fs (see Figs. S1 (a) and S1 (e)). However,

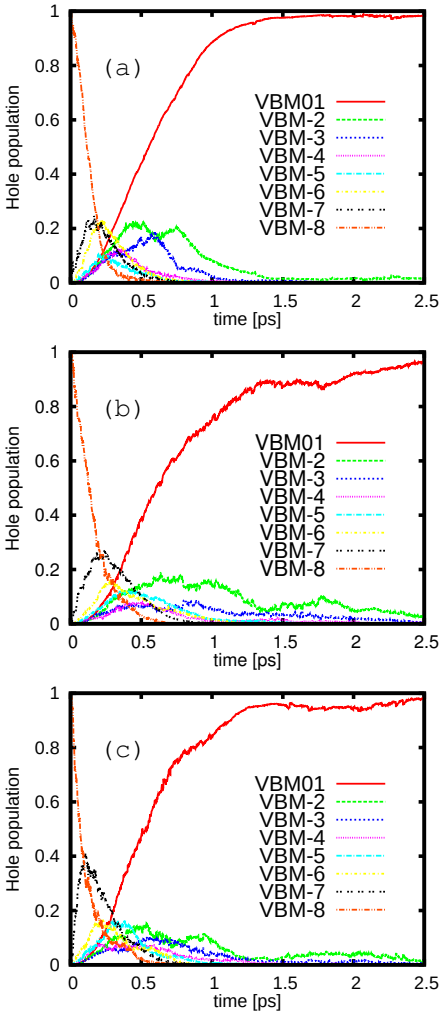

Fig. 5 Time evolution of the hole state populations when initially starting from the excited state VBM-8 for T-$MAPbI_3$ (a), T-$MAPbI_3$(Cl) (b), and T-$MAPbI_3$(Br) (c).

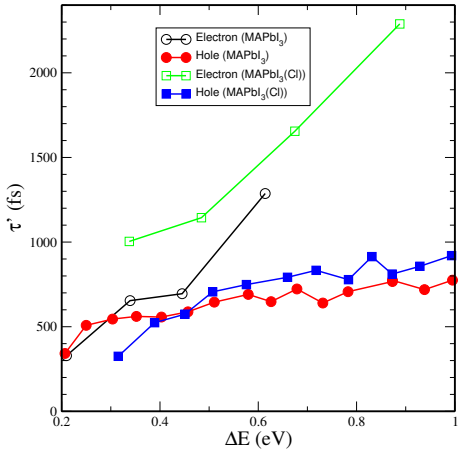

Fig. 6 Population time τ' (fs) of the lowest two electronic states (Pop(CBM01) = Pop(CBM) + Pop(CBM+1)) when initially populating different electron/hole excited states and for two perovskite systems.

the effect of Cl substitution on the relaxation time of the hot holes is not as pronounced as in the case of the hot electrons: a small increase in the carrier relaxation time is obtained only at larger excitation energies (compare open circles and open squares in Fig. 6). A pronounced asymmetry in electron and hole relaxation dynamics is seen in the case of Cl substitution. As an example, for an excitation energy of 0.5 eV, $\tau'_e \approx 1160$ fs compared to $\tau'_h \approx 700$ fs. At an energy $\Delta E \approx 0.89$ eV, the population time for electrons is about 2290 fs which is more than 2.5 times larger than the population time for holes ($\tau'_h \approx 840$ fs). We also found that the effect of partial Br substitution on the relaxation time of the charge carriers is not as pronounced as in the case of partial Cl substitution (see Figs. S1 (d) and S1 (i)): only a small overall increase of the relaxation time is obtained. For comparison, we have also considered full Cl and Br substitution (see Fig. S1). Despite a considerable increase in the charge carrier relaxation in the partially chlorinated system, full chlorination hinders this effect, with characteristic decay times comparable to or sometimes lower than the full iodine perovskite. In fact, the hot electron relaxation becomes faster in T-$MAPbCl_3$ system as compared to the full iodide system for most of the excitation energies (Figs. S1 (c) and S1 (h)). Full bromination (T-$MAPbBr_3$) also results in a small overall increase of the relaxation time. For all the considered systems, the hole relaxation time show a less pronounced energy dependence compared to the electron relaxation time. This could be due to the denser hole states, which result in stronger NA couplings and therefore more delocalized hole character.

In order to have a better representation of the exciton energy dependence of the hot-electron relaxation, we show in Fig.7 a two-dimensional (2D) plot of the electron relaxation dynamics T-$MAPbI_3$ and T-$MAPbI_3$(Cl) from the CBM+4 state. Such 2D phase diagrams, which represent the probability (z-axis) of finding the system at a given energy (y-axis) at a given time (x-axis), offer a good tool for representing and analyzing the dynamics. It is particularly useful in our case since we have materials with different spacing between the excited states. Note that in plotting this 2D representation, the energy of the ground state configuration is taken as the energy reference. Figure 7 clearly shows the fast electron relaxation on a timescale of $\sim$ 500 fs for $MAPbI_3$. This relaxation is followed by a very slow decay that corresponds to a constant population of the conduction band edge state. The lower part of the figure represents the relaxation dynamics of T-$MAPbI_3$(Cl). As is evident from the figure, a strong slowdown in the relaxation process is seen compared to T-$MAPbI_3$: the electron relaxation occurs on a timescale of $\sim$ 1500 fs. This shows clearly the effect of mixing with Cl on slowing down the electron

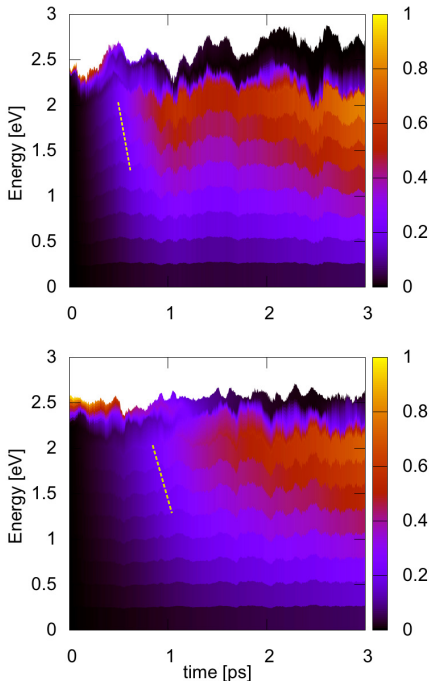

Fig. 7 2D map representing the electron relaxation dynamics where the surface hopping (SH) based populations of all basis states (with energy $\leq$ 0.5 eV below the CBM) as a function of their energy and time for $MAPbI_3$ (Top panel) and T-$MAPbI_3$(Cl) (Bottom panel). Various excited state configurations obtained by promoting an electron from the VBM to CBM+n (n=1,2, .. 5 for $MAPbI_3$ and n=1,2, .. 4 for T-$MAPbI_3$(Cl)) are considered. Here the ground state energy is taken as a reference energy. The dotted line serves as a guide to the eye.

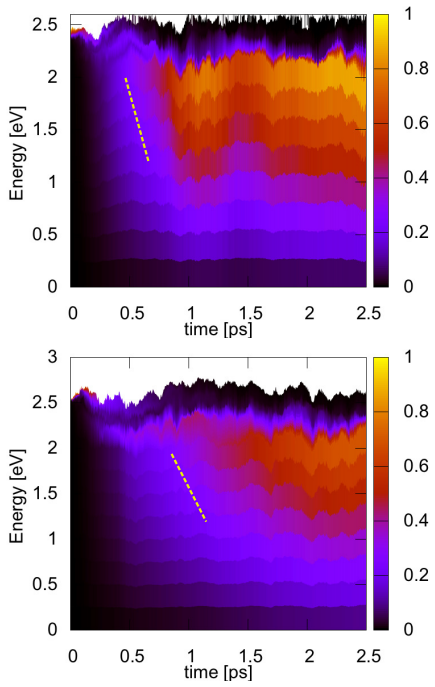

Fig. 8 2D map representing the hole relaxation dynamics where the SH-based populations of all basis states(with energy $\leq$ 0.5 eV below the VBM) as a function of their energy and time for $MAPbI_3$ (Top panel) and T-$MAPbI_3$(Cl) (Bottom panel). Various excited state configurations obtained by promoting an electron from the VBM-n to CBM (n=1,2, .. 8 for $MAPbI_3$ and n=1,2, .. 7 for T-$MAPbI_3$(Cl)) are considered. Here the ground state energy is taken as a reference energy. The dotted line serves as a guide to the eye.

relaxation dynamics.

Similarly, Fig. 8 shows the hole relaxation dynamics of $MAPbI_3$ and T-$MAPbI_3$(Cl), which also shows the positive effects of the Cl substitution on the relaxation of the holes. As we already mentioned, holes decay faster than electrons to the band edge, especially in T-$MAPbI_3$(Cl), leading to a larger concentration of accumulated positive charges at the band edge. Therefore we predict that positive charge accumulation in mixed-halide perovskites is more pronounced than in pure iodide perovskite.

The projected density of states (pDOS) for $MAPbI_3$, T-$MAPbI_3$(Cl) and T-$MAPbI_3$(Br) is shown in Fig.9, and it explains the origin of the weak couplings in T-$MAPbI_3$(Cl). At energies close to the VBM, the states of T-$MAPbI_3$ consist mainly of I(5p) orbitals with an overlapping between Pb(6p) and Pb(6s). At energies close to the CBM, the pDOS is formed by the Pb(6p), I(5p) and I(5s) orbitals. For T-$MAPbI_3$(Cl), the CB pDOS has a contribution from the Cl(3p) orbitals, and similarly there is a contribution from Br(3p) states in the CB for T-$MAPbI_3$(Br). As a result, the Pb states at the CBM show notable hybridisation with Cl states, as shown in Fig. 9b. The molecular orbitals for T-$MAPbI_3$(Cl) are irregular, so there will be more cancellation of the overlaps (negative vs positive) in comparison to T-$MAPbI_3$ that result in smaller NACs in T-$MAPbI_3$(Cl) (see Tables S1 and S2, SI).

Figure S2 (SI) shows the influence spectra for electron-phonon relaxation from different excited states in three perovskite systems. It is evident from the figure that electrons in $MAPbI_3$ and T-$MAPbI_3$(Br) couple more strongly to higher frequency modes than electrons in T-$MAPbI_3$(Cl). This will lead to a faster electron decay in $MAPbI_3$ and T-$MAPbI_3$(Br) compared to $MAPbI_3$(Cl). For the pDOS of the three perovskite systems shown in Figure 9, the valence band is dominated by the contribution from the I(5p) states. Therefore, the NACs between valence states are expected to be similar for doped and undoped systems. A High density of states implies closeness between the energies of VB orbitals. As a result, the interaction of nearly-degenerate orbitals is expected to be large, leading to larger NACs.

The electron localisation function (ELF) is a useful tool to study electronic structure, especially for chemical bonding states. In Fig.10, ELF of the $MAPbI_3$ and T-$MAPbI_3$(Cl) are plotted and compared. For Chlorine substitution, there is a little less over-

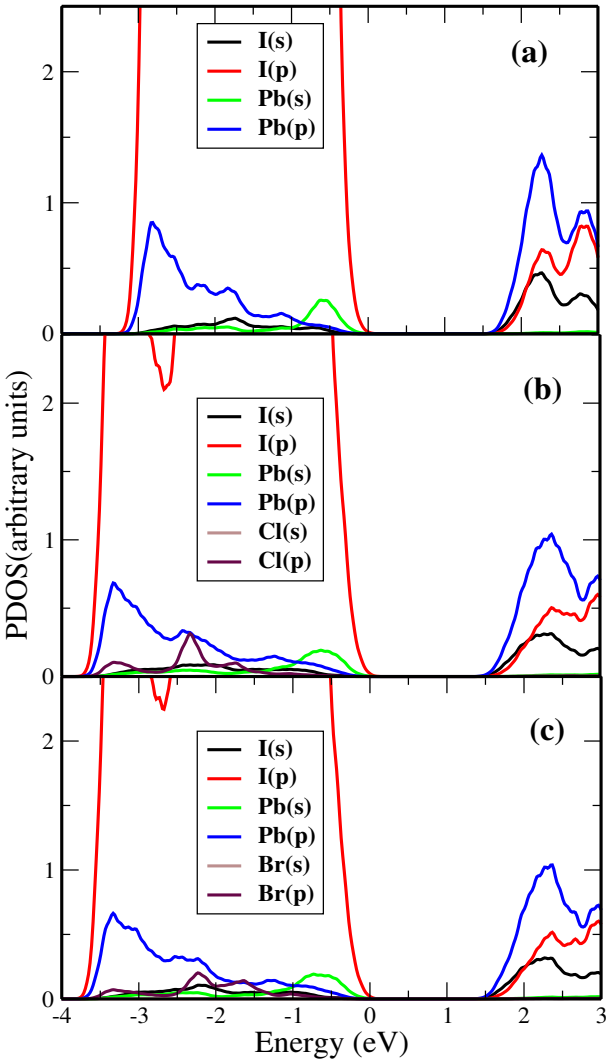

Fig. 9 Projected density of states pDOS for (a) $MAPbI_3$ (b) T-$MAPbI_3$(Cl) and T-$MAPbI_3$(Br) (c).

lap between the electronic density of Cl and Pb atoms as compared to the case of full iodide system. This is mainly due to the asymmetry introduced by out of plane displacement of the Pb atom in $MAPbI_3$(Cl). We found that Cl doping induces important structural deformation of the PbI_6 octahedra removing the inversion symmetry. In pristine $MAPbI_3$ the octahedra are non distorted and possess inversion symmetry but only rotate by 17 degrees with respect to their neighbors. However the inversion symmetry is broken in the case of Cl doping at equatorial site. In T-$MAPbI_3$(Cl) the rotation of the PbI_6 octahedra reduced to 4 degrees. However, the octahedra are now significantly distorted and asymmetric. The three in plane I-I distances are 4.35 Å except one Cl-I bond is 4.45 Å. In addition, the Pb atom is displaced from the center of octahedron. Such a displacement can originate from the stronger electronic density localized around Cl. A measurement of the apical Pb-I distance leads to two different bond lengths of 3.37 and 4.1 Å , respectively. The inversion symmetry breaking also lifts the degeneracy of the bands as we observed from band structure analysis.

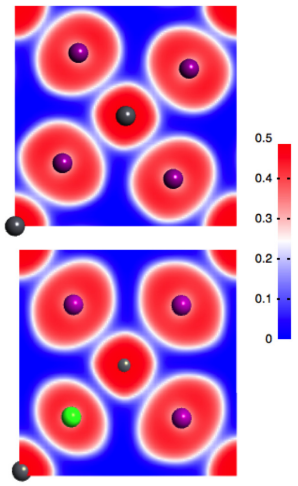

Fig. 10 Electron localisation function (ELF) contour plots on the basal plane obtained for T-$MAPbI_3$ (Top panel) and T-$MAPbI_3$(Cl) (Bottom panel).

The NACs are related to the rate of change of orbital overlaps as a result of nuclear motion. Consequently, a large absolute value of the molecular orbital overlaps often leads to larger NACs. As a result, it can be expected that the VB states are coupled to each other more strongly than the CB states. Our findings support this argument, showing VB couplings to be up to an order of magnitude larger than those of the CB (see Tables S1 and S2, SI). These results explain the faster hole relaxation in comparison to electron relaxation. The present analysis of the pDOS also explains the dependence of hole relaxation dynamics on halide composition.

Recently, Xing et al. reported that hot holes created at an energy $\sim$ 1 eV below the VBM relax to the band edge of the valence band within $\sim$ 400 fs[15]. Using time-resolved transient absorption studies, Piatkowski et al.[83] observed that hot electron and hot hole relaxation times within perovskite conduction and valence bands are 700 and 600 fs, respectively. Our data in Fig.11 indicate that hot hole (with energy $\leq$ 1.0 eV below the VBM) relaxation near the band edge of the valence band is characterized by a relaxation time of about 700 fs which is in good agreement with the experimental value reported in ref.[83].

Pure as well as mixed-halide perovskites have been successfully used in solar cell devices and showed high efficiency, but on the other hand the incorporation mechanism of chlorine into the pure iodide perovskite and its effect are still a matter of debate. Dha-

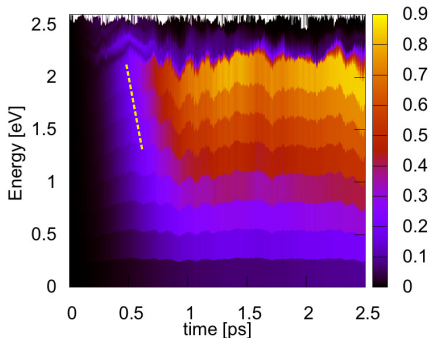

Fig. 11 2D map representing the hot hole relaxation dynamics where the SH-based populations of all basis states (with energy $\leq$ 1.0 eV below the VBM) as a function of their energy and time for $MAPbI_3$. The first 18 excited state configurations obtained by promoting an electron from the VBM-n to CBM are considered. The the energy of the ground state configuration is taken as reference energy.

rani et al.[34], have shown that the addition of low amounts of Cl leads to an increase in the perovskite conductivity and therefore improves the solar cell performance. Wehrenfennig et al.[25] attributed the improved performance of $MAPbI_{3-x}Cl_x$ mixed-halide perovskite compared to that of $MAPbI_3$ to lower charge recombination rates rather than to better charge mobility. Our present work suggests that doping with low amounts of Cl has a strong impact on slowing down the electron and hole relaxation dynamics. As a consequence, the life time of initially generated exciton is increased, leading to a better chances on charge separation. In addition, the asymmetry in electron and hole relaxation dynamics may also contribute to lowering electron-hole recombination rates.

2.4 Spectral density

To gain insight into the type of vibronic modes that drive the non-radiative energy relaxation in perovskites, we have computed the influence spectrum for all considered systems. The computations are based on the optical response formalism, as detailed elsewhere[74,84–86]. The influence spectra are similar to IR or phonon DOS spectra, except that they show only the modes responsible for each particular electronic transition. The computed influence spectra for the pure iodide perovskite are shown in Figure 12a and Figure 12b for electron and hole relaxations, respectively. The influence spectrum is calculated by taking the Fourier transform of the time-dependent energy gap autocorrelation function for a pair of electronic/hole states. For the electron influence spectrum, an intense peak is seen around 85 cm^{-1}. Other less pronounced peaks in frequency range between 200 and 600 cm^{-1} are also present, especially for $MAPbI_3$. The amplitude of the peaks in the influence spectrum corresponds to the electron-phonon (hole-phonon) coupling strength at that frequency. The influence spectrum for hole relaxation shows similar frequencies. The nature of the vibration modes in perovskite materials has already been investigated in a few recent publications as we discuss in the following.

In Ref.[87], it was reported that the high-frequency modes are associated with vibrational modes of the molecular cation. The lowest frequency modes (below 150 cm^{-1}) arise mainly from the inorganic cage, but with half of the modes coupled to the motion of the MA molecule. Quarti el al.[88] reported experimentally measured Raman spectra, and they calculated the spectra for various structural phases of T-$MAPbI_3$ and identified the origin of the most important frequencies.

Figure 12a illustrates the influence spectra for electron relaxation, which is dominated by contributions from modes around 100 cm^{-1} and attributed to the inorganic cage modes. Contributions from high frequency modes are also present at frequencies between 200 and 600 cm^{-1}. As mentioned before, these high-frequency modes are attributed to the motion of the MA molecules and to coupled modes between the organic and inorganic parts. Figure 12b shows that the influence spectra for hole relaxation are not dominated only by contributions from a mode around 100 cm^{-1}, as the case of electron relaxation, but also contain contributions from higher frequency modes. A dominant one of these additional modes has a frequency near 150 cm^{-1}, which corresponds to Pb-I bond stretching and MA twisting (a collective motion). The MA molecular vibration and motion is widely accepted to play a crucial role in the electronic properties of T-$MAPbI_3$[89,90]. For example, Motta el al.[90] demonstrated that the MA full rotation induced by temperature fluctuations could affect the VBM and CBM edges even prohibiting carrier recombination. The T-$MAPbI_3$ behaves as a direct band gap semiconductor while the molecular motion prohibits the radiative recombination, thus contributing to the accumulation of charge at the band edges. Zheng et al.[63] identified the phonon modes that contribute most to the carrier relaxation. These modes were attributed mainly to the MA molecule, such as MA translation, CH/NH bond twisting and CH/NH stretching. Our simulations indicate an important role of the MA molecule in the carrier relaxation dynamics.

3 Conclusions

In conclusion, motivated by recent experimental studies on carrier transport and thermalization, we have investigated hot carrier relaxation dynamics in mixed-halide perovskites using first-principle methods. We have identified the ultrafast charge carrier cooling process and determined the relaxation time for both electrons and holes for a wide range of excitation energies. For the lead iodide perovskite, our results show that electrons excited up to 0.5 eV above the CBM and holes created up to 1.0 eV below the VBM relax within $\sim$ 700 fs, in agreement with recent experimental results. Hole relaxation is found to be faster than

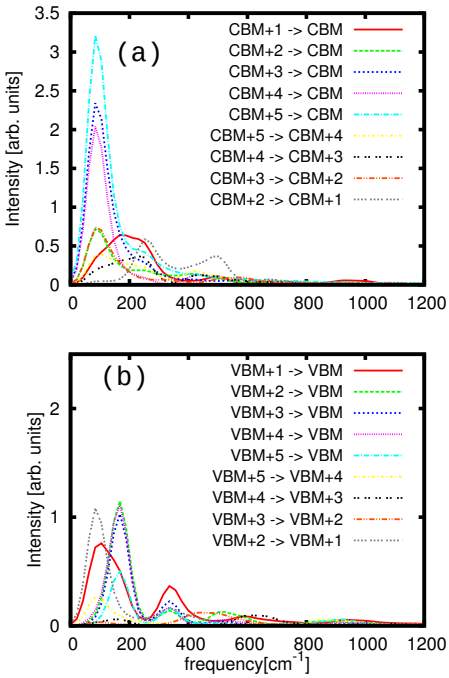

Fig. 12 Influence spectrum for the electron-phonon (a) and hole-phonon (b) relaxation from different excited states in $MAPbI_3$.

electron relaxation and this difference is more pronounced for the Cl doped material. Based on the results of our calculations, we attribute this difference to larger NA couplings between valence band states compared to those between conduction band states. This asymmetry in electron and hole relaxation dynamics may also contribute to lowering electron-hole recombination rates. We also found that halide mixing with Cl at low concentrations leads to slowing down the electron and hole relaxation dynamics. This is due to the reduced NAC in the system originating from the charge state localization around the Cl atom. Our analysis of the spectral density shows that electron and hole relaxation is driven mainly by low-frequency modes related to I and Pb ion motions. There is also a contribution from high frequency modes related to MA ion motion and to coupled modes between organic and inorganic parts. We showed that slowing down the hot carrier thermalization dynamics can be realized by considering simple methods based on chloride doped perovskite materials. These results will help guide future work on how the phonon modes in different materials can affect hot carrier relaxation.

4 ACKNOWLEDGMENTS

M.E.M. thanks S. Hoogland and O. Voznyy for their careful reading of the manuscript and helpful comments. Computational resources have been provided by the research computing center at Texas A&M University in Qatar.

References

1 G. Xing, N. Mathews, S. S. Lim, N. Yantara, X. Liu, D. Sabba, M. Grätzel, S. Mhaisalkar, and T. C. Sum, Nat. Mater., 2014, **13**, 476.

2 National Renewable Energy Laboratory, Best Research-Cell Efficiencies; www.nrel.gov/ncpv/images/efficiency_chart.jpg.

3 M. A. Green, A. Ho-Baillie, and H. J. Snaith, Nat. Photonics, 2014, **8**, 506.

4 J. Gong, S. B. Darling and F. You, Energy Environ. Sci., 2015, **8**, 1953.

5 T. C. Sum and N. Mathews, Energy Environ. Sci., 2014, **7**, 2518.

6 P. Gao, M. Grätzel, and M. K. Nazeeruddin, Energy Environ. Sci., 2014, **7**, 2448.

7 H. Zhou, Q. Chen, G. Li, S. Luo, T.-b. Song, H.-S. Duan, Z. Hong, J. You, Y. Liu, and Y. Yang, Sience, 2014, **345**, 542.

8 S. A. Bretschneider, J. Weickert, J. A. Dorman, and L. Schmidt-Mende, APL Mater. , 2014, **2**, 040701.

9 J. H. Heo, H. J. Han, D. Kim, T. K. Ahn and S. H. Im, Energy Environ. Sci., 2015, **8**, 1602.

10 I E. Castelli, K. S. Thygesen and K. W. Jacobsen, Energy Environ. Sci., 2015, **3**, 12343.

11 P. Umari, E. Mosconi, and F. De Angelis, Sci. Rep., 2014, **4**, 4467.

12 J. M. Frost, K. T. Butler, F. Brivio, C. H. Hendon, and M. van Schilfgaarde, Nano Lett., 2014, **14**, 2584.

13 J. M. Frost, K. T. Butler, A. Walsh, and M. van Schilfgaarde, Phys. Rev. B, 2014, **89**, 155204.

14 W. J. Yin, T. Shi, and Y. Yan, Adv. Mater., 2014, **26**, 4653.

15 G. Xing, N. Mathews, S. Sun, S. S. Lim, Y. M. Lam, M. Grätzel, S. Mhaisalkar, and T. C. Sum, Science, 2013, **342**, 344.

16 S. D. Stranks, G. E. Eperon, G. Grancini, C. Menelaou, M. J. Alcocer, T. Leijtens, L. M. Herz, A. Petrozza, and H. J. Snaith, Science, 2013, **342**, 341.

17 Q. Dong, Y. Fang,Y. Shao, P. Mulligan, J. Qiu, L. Cao, J. Huang, Science, 2015, **347**, 967.

18 Y. X. Zhao, A. M. Nardes, and K. Zhu, J. Phys. Chem. Lett., 2014, **5**, 490.

19 D. Shi, V. Adinolfi, R. Comin, M. Yuan, E. Alarousu, A. Buin, Y. Chen, S. Hoogland, A. Rothenberger, K. Katsiev, Y. Losovyj, X. Zhang, P. A. Dowben, O. F. Mohammed, E. H. Sargent, O. M. Bakr, Science, 2015, **347**, 519.

20 F. Brivio, A. B. Walker, and A. Walsh, APL Materials , 2013, **1**, 042111.

21 G. Giorgi, J.-I.Fujisawa, H. Segawa, and K. Yamashita, J. Phys. Chem. Lett., 2013, **4**, 4212.

22 Y. X. Zhao and K. Zhu, J. Phys. Chem. Lett., 2013, **4**, 2880.

23 J. Feng and B. Xiao, J. Phys. Chem. Lett., 2014, **5**, 1278.

24 M. H. Du, J. Mater. Chem., 2013, **4**, 4213.

25 C. Wehrenfennig, G. E. Eperon, M. B. Johnston, H. J. Snaith, and L. M. Herz, Adv. Mater., 2014, **26**, 1584.

26 W. J. Yin, T. Shi, and Y. Yan, Apl. Phys. Lett., 2014, **104**, 063903.

27 J. Kim, S. H. Lee, J. H. Lee, and H. K. Hong, J. Phys. Chem Lett., 2014, **5**, 1312.

28 S. Colella, E. Mosconi, P. Fedeli, A. Listorti, F. Gazza, F. Orlandi, P. Ferro, T. Besagni, A. Rizzo, G. Calestani, G. Gigli, F. De Angelis, and R. Mosca, Chem. Mater., 2013, **25**, 4613.

29 E. Mosconi, A. Amat, Md. K. Nazeeruddin, M. Grätzel, and F. De Angelis, J. Phys. Chem. C, 2013, **117**, 13902.

30 J. H. Noh, S. H. Im, J. Heo, T. N. Mandal, and S. I. Seok, Nano. Lett., 2014, **13**, 1764.

31 A. Amat, E. Mosconi, E. Ronca, C. Quarti, P. Umari, M. K. Nazeeruddin, M. Graetzel, and F. De Angelis, Nano Lett., 2014, **14**, 3608.

32 W.-J. Yin, Y. Yan, and S.-H. Wei, J. Phys. Chem. Lett., 2014, **5**, 3625.

33 M. Zhang, H. Yu, M. Lyu, Q. Wang, J.-H. Yun, and L. Wang, Chem. Commun., 2014, **50**, 11727.

34 S. Dharani, H. A. Dewi, R. R. Prabhakar, T. Baikie, C. Shi, D. Yonghua, N. Mathews, P. P. Boix, and S. G. Mhaisalkar, Nanoscale, 2014, **6**, 13854.

35 S. T. Williams, F. Zuo, C.-C. Chueh, C.-Y. Liao, P.-W. Liang, and A. K.-Y. Jen, ACS Nano, 2014, **8**, 10640.

36 E. T. Hoke, D. J. Slotcavage, E. R. Dohner, A. R. Bowring, H. I. Karunadasa, and M. D. McGehee, Chem. Sci.,2015, **6**, 613.

37 N. J. Jeon, J. H. Noh, W. S. Yang, Y. C. Kim, S. Ryu, J. Seo, and S. Seok, Nature (London), 2015, **517**, 476.

38 W. Nie, H. Tsai, R. Asadpour, J.-C. Blancon, A. J. Neukirch, G. Gupta, J. J. Crochet, M. Chhowalla, S. Tretiak, M. A. Alam, H.-L. Wang, A. D. Mohite, Science, 2015, **347** 522.

39 M. M. Lee, J. Teuscher, T. Miyasaka, T. N. Murakami, and H. J. Snaith, Science, 2012, **338**, 643.

40 A. Buin, P. Pietsch, J. Xu, O. Voznyy, A. H. Ip, R. Comin, and E. H. Sargent, Nano Lett.,2014, **14**, 6281.

41 E. Edri, S. Kirmayer, M. Kulbak, G. Hodes, and D. Cahen, J. Phys. Chem. Lett., 2014, **5**, 429.

42 E. Edri, S. Kirmayer, A. Henning, S. Mukhopadhyay, K. Gartsman, Y. Rosenwaks, G. Hodes, and D. Cahen, Nano Lett., 2014, **14**, 1000.

43 F. Zheng, H. Takenaka, F. Wang, N. Z. Koocher, and A. M. Rappe, J. Phys. Chem. Lett. 2015, **6**, 31.

44 T. J. Savenije, C. S. Ponseca, Jr., L. Kunneman, M. Abdellah, K. Zheng, Y. Tian, Q. Zhu, S. E. Canton, I. G. Scheblykin, T. Pullerits, A. Yartsev, and V. Sundstrom, J. Phys. Chem. Lett., 2014, **5**, 2189.

45 C. Wehrenfennig, M. Liu, H. J. Snaith, M. B. Johnston, and L. M. Herz, J. Phys. Chem. Lett.,2014, **5**, 1300.

46 C. Wehrenfennig, M. Liu, H. J. Snaith, M. B. Johnston, and L. M. Herz, Apl. Materials, 2014, **2**, 081513.

47 J. M. Ball, S. D. Stranks, M. T. Hörantner, S. Hüttner, W. Zhang, E. J. W. Crossland, I, Ramirez, M. Riede, M. B. Johnston, R. H. Friend and H. J. Snaith, Energy Environ. Sci., 2015, **8**, 602.

48 J. M. Azpiroz, E. Mosconi, J. Bisquert and F. De Angelis, Energy Environ. Sci., 2015, **8**, 2118.

49 C. X. Sheng, C. Zhang, Y. Zhai, K. Mielczarek, W. Wang, W. Ma, A. Zakhidov, and Z. V. Vardeny, Phys. Rev. Lett., 2015, **114**, 116601.

50 A. Miyata, A. Mitioglu, P. Plochocka, O. Portugall, J. T. Wang, S. D. Stranks, H. J. Snaith, R. J. Nicholas, Nat. Phys., 2015, **11**, 582.

51 H. Hsu, C. Wang, A. Fathi, J. Shiu, C. Chung, P. Shen, T. Guo, P. Chen, Y. Lee, and E. Diau, Angew. Chem., 2014, **53**, 1.

52 R.T. Ross and A. J. Nozik, J. Apl. Phys., 1982, **53**, 3818.

53 G. Conibeer, R. Patterson ,L. Huang, J. F. Guillemoles,D. König, S. Shrestha, M. A. Green Sol. Energ. Mat. Sol. C., 2010, **94**, 1516.

54 S. Saeed, E.M.L.D. de Jong, K. Dohnalova and T. Gregorkiewicz, Nat. commun., 2014, **5**, 4665.

55 Y. Yang, D. P. Ostrowski, R. M. France, K. Zhu, J. van de Lagemaat, J.M. Luther and M. C. Beard, Nat. Photonics, 2015, doi:10.1038/nphoton.2015.213

56 M. B. Price, J. Butkus, T. C. Jellicoe, A. Sadhanala, A. Briane, J. E. Halpert, K. Broch, J. M. Hodgkiss, R. H. Friend and F. Deschler, Nat. commun., 2015, **6**, 8420.

57 A. Marchioro, J. Teuscher, D. Friedrich, M. Kunst, R. van de Krol, T. Moehl, M. Grätzel, J.-E. Moser, Nat. Photonics, 2014, **8**, 250.

58 C. Wehrenfennig, M. Liu, H. J. Snaith, M. B. Johnston and L. M. Herz, Energy Environ. Sci., 2014, **7**, 2269.

59 H.Kawai, G. Giorgi, A. Marini, and K. Yamashita, Nano Lett., 2015, **15**, 3103.

60 J. A. Christians, J. S. Manser, and P. V. Kamat, J. Phys. Chem. Lett., 2015,**6**, 2086.

61 M. T. Trinh, X. Wu, D. Niesner and X.-Y. Zhu, J. Mater. Chem. A , 2015, **3**, 9285.

62 R. Nanguneri and J. Parkhill, arXiv:1411.1110

63 F. Zheng, L. Z. Tan, S. Liu, and A. M. Rappe, Nano Lett., 2015, **15**, 7794.

64 K. Chen, A. J. Barker, F. L. C. Morgan, J. E. Halpert, and J.

M. Hodgkiss, J. Phys. Chem. Lett., 2015, **6**, 153.
65 K. G. Stamplecoskie, J. S. Manserab and P. V. Kamat, Energy Environ. Sci., 2015, **8**, 208.
66 J.S. Manser and P. V. Kamat, Nat. Photonics, 2014, **8**, 737.
67 P. Umari, E. Mosconi and F. De Angelis, Sci. Rep., 2013, **4**, 4467.
68 J.C. Tully, J. Chem. Phys., 1990, **93**, 1061.
69 L. Verlet Phys. Rev., 1967, **159**, 98.
70 W.C. Swope, H.C. Andersen, P.H. Berens, and K.R. Wilson, J. Chem. Phys.,1982, **76**, 637.
71 S. Hammes-Schiffer and J. C. Tully, J. Chem. Phys., 1994, **101**, 4657).
72 X. Zhang, Z. Li, and G. Lu, Phys. Rev. B, 2010, **82**, 205210.
73 A.V. Akimov, O.V. Prezhdo, J. Chem. Theory Comput., 2014, **10**, 789.
74 A.V. Akimov, O.V. Prezhdo, J. Chem. Theory Comput., 2013, **9**, 4959.
75 A. V. Akimov, A. J. Neukirch, and O. V. Prezhdo, Chem. Rev., 2013, **113**, 4497.
76 J.P. Perdew, K. Burke, M. Ernzerhof, Phys. Rev. Lett.,1996, **77**, 3865.
77 J.P. Perdew, K. Burke, M. Ernzerhof, Phys. Rev. Lett., 1997, **78**, 1396.
78 Gianozzi, P.; Baroni, S.; Bonini, N.; Calandra, M.; Car, R.; Cavazzoni, C.; Ceresoli, D.; Chiarotti, G. L.; Cococcioni, M.; Dabo, I.; Dal Corso, A.; de Gironcoli, S.; Fabris, S.; Fratesi, G.; Gebauer, R.; Gerstmann, U.; Gougoussis, C.; Kokalj, A.; Lazzeri, M.; Martin-Samos, L.; Marzari, N.; Mauri, F.; Mazzarello, R.; Paolini, S.; Pasquarello, A.; Paulatto, L.; Sbraccia, C.; Scandolo, S.; Sclauzero, G.; Seitsonen, A. P.; Smogunov, A.; Umari, P.; Wentzcovitch, R. M. QUANTUM ESPRESSO: A Modular and Open-Source Software Project for Quantum Simulations of Materials. J. Phys. Condens. Matter, 2009, **21**, 395592.
79 H.C. Andersen, J. Chem. Phys., 1980, **72**, 2384.
80 C. Craig, W. Duncan, and O. Prezhdo, Phys. Rev. Lett.,2005,**95**, 163001.
81 M. Bernardi, D. Vigil-Fowler, J. Lischner, J. B. Neaton and S. G. Louie, Phys. Rev. Lett., 2014, **112**, 257402.
82 E. Mosconi, A. Amat, Md.K. Nazeeruddin, M. Grätzel, F. De Angelis, J. Phys. Chem. C, 2013, **117**, 13902.
83 P. Piatkowski, B.Cohen, F. J. Ramos, M.Di Nunzio, M. K. Nazeeruddin, M. Grätzel, S.Ahmad and A.Douhal, Phys. Chem. Chem. Phys., 2015, **17**, 14674.
84 S. Mukamel, Principles of Nonlinear Optical Spectroscopy; Oxford University Press: New York, 1995.
85 A.B. Madrid, K. Hyeon-Deuk, B.F. Habenicht, and O.V. Prezhdo, ACS Nano, 2009, **3**, 2487.
86 A.V. Akimov and O.V. Prezhdo, J. Phys. Chem. Lett., 2013, **4**, 3857.
87 F. Brivio, J. M. Frost, J. M. Skelton, A. J. Jackson, O. J. Weber, M.T. Weller, A. R. Goni, A. M. A. Leguy, P. R. F. Barnes, A. Walsh, Phys. Rev. B, 2015, **92**, 144308.
88 C. Quarti, G. Grancini, E. Mosconi, P. Bruno, J.M. Ball, M.M. Lee, H.J. Snaith, A. Petrozza and F. De Angelis, J. Phys. Chem. Lett., 2014, **5**, 279
89 M.A. Carignano, A. Kachmar and J. Hutter, J. Phys. Chem C, 2015, **119**, 8991.
90 C. Motta, F. El-Mellouhi, S. Kais, N. Tabet, F. Alharbi, S. Sanvito, Nat. commun., 2015, **6**, 7026.